

# Flexible design of building integrated thin-film photovoltaics

Nils Neugebohrn<sup>1</sup>  | Stefan Haas<sup>2</sup> | Andreas Gerber<sup>2</sup> | Michael Grimm<sup>3</sup> |  
Jana Nissel<sup>3</sup> | Rene Liebers<sup>3</sup> | Bugra Turan<sup>4</sup> | Kai Gehrke<sup>1</sup> | Martin Vehse<sup>1</sup>

<sup>1</sup>Urban and Residential Technologies, DLR Institute of Networked Energy Systems, Oldenburg, Germany

<sup>2</sup>EK5 – Photovoltaik, Forschungszentrum Jülich GmbH, Jülich, Germany

<sup>3</sup>3D-Micromac AG, Chemnitz, Germany

<sup>4</sup>Rheinische Fachhochschule Köln, Cologne, Germany

## Correspondence

Nils Neugebohrn, Urban and Residential Technologies, DLR Institute of Networked Energy Systems, Carl-von-Ossietzky-Str. 15, 26129 Oldenburg, Germany.  
Email: [nils.neugebohrn@dlr.de](mailto:nils.neugebohrn@dlr.de)

## Funding information

BMWf, Grant/Award Number: FKZ0324130A

## Abstract

The high cost of building integrated photovoltaics is one of the main reasons preventing a more widespread application. We propose a panel-on-demand concept for flexible design of building integrated thin-film photovoltaics to address this issue. The concept is based on the use of semi-finished PV modules (standard mass products) with subsequent refinement into BIPV PV modules. In this study, we demonstrate the three processes necessary to realize this concept. First, a prototype tool to cut thin film photovoltaic elements on glass substrates based on laser perforation was developed. Damage to the processed samples did not exceed a distance of 50  $\mu\text{m}$  from laser cuts. Second, oxide/metal/oxide-electrodes with integrated colour were applied on Cu (In, Ga)Se<sub>2</sub> cells and standard monolithic interconnection structuring was used to produce modules sized 30  $\times$  30 cm<sup>2</sup> in red, green and blue with strong colours. Third, A back-end interconnection process was developed for amorphous silicon thin film cells, which allows for the structuring of modules from elements of custom shape. The panel-on-demand strategy may allow for a streamlined production of customized modules and a lower cost for aesthetically pleasing, fully building integrated solar modules.

## KEYWORDS

back-end interconnection, building integrated photovoltaics (BIPV), coloured solar modules, custom size solar modules, customized modules

## 1 | INTRODUCTION

Buildings account for 40% of global energy consumption.<sup>1</sup> To reduce this, building-integrated PV (BIPV) can play an important role by opening new areas for photovoltaics. Despite all efforts in recent years by developing new BIPV products and inspiring best practice examples, BIPV is still a niche market in Germany.<sup>2</sup> This could change with an amendment of the new building standard. A regulation for obligatory installation of solar devices has already been introduced in the federal state of Berlin and is also being discussed as a national requirement,<sup>3</sup> which could lead to an upswing for BIPV. According to a recent study by Eggers et al the potential for façade BIPV is twice as large as the potential for roofs and is reported to be 12,000 km<sup>2</sup>, which underlines

the theoretical potential of the building envelope for energy generation in Germany.<sup>2</sup>

To increase the market penetration of BIPV products, a number of factors need to fit together: There is the need (mostly by architects) for design flexibility of photovoltaic façade systems in terms of size, colour scheme, design and cladding systems. This flexibility leads to higher production costs compared to standardized systems. Another disadvantage of non-standardized BIPV façade elements are building codes, which can cause high costs for tests regarding mechanical, electrical, as well as fire safety. In addition, these tests are time-consuming. In the end, the cost comparison between a BIPV and a conventional façade is what counts. A detailed analysis of the costs and a BIPV market overview is listed in the review article by Tilman E. Kuhn published in 2020<sup>4</sup> and

This is an open access article under the terms of the [Creative Commons Attribution-NonCommercial](https://creativecommons.org/licenses/by-nc/4.0/) License, which permits use, distribution and reproduction in any medium, provided the original work is properly cited and is not used for commercial purposes.

© 2022 The Authors. Progress in Photovoltaics: Research and Applications published by John Wiley & Sons Ltd.

the BIPV status report 2020 published by the Becquerel Institute and SUPSI.<sup>5</sup> While for standard PV systems, the levelized cost of electricity is the most important parameter in terms of costs, it is more complicated in case of a BIPV product. Here, the BIPV product must compete with additional parts of the building envelope such as the cost of a standard non-PV cladding system. The cost analysis of the component costs of ventilated and non-ventilated BIPV facades of different technologies in comparison to the component costs of regular facades is shown in the BIPV status report 2020.<sup>5</sup> The study concludes that both ventilated and non-ventilated BIPV facades are in most cases still more expensive than the non-PV facades. Only in the case of ventilated facades can a CIGS BIPV facade keep up with a regular insulating glass or a regular stone facade in terms of costs.<sup>5</sup>

From a technological point of view, two PV technologies can generally be considered for BIPV applications: Wafer technologies, which currently dominate the global PV market, and thin-film technologies such as Cu (In, Ga)Se<sub>2</sub> (CIGS) and organic photovoltaics (OPV), which play a niche role but still have high potential in terms of efficiency.<sup>6</sup> Thin-film technologies can play a more important role in BIPV applications, as we will demonstrate in this paper using the 'panel-on-demand concept'. We focus here on the technological aspects on how to increase the flexibility and reduce the price.

The panel-on-demand concept for flexible design of building integrated thin-film photovoltaics is visualized in Figure 1. In the first step, thin-film solar modules (e.g., CIGS) are produced as semi-finished products or semi-fabricates in large quantities on large glass plates. These are then shipped to refinement centres positioned in the consumer markets. There, the modules are refined into customized solar modules according to size, shape and colour on demand according to customer specifications in the second step. The refinement can be achieved using methods already used in the glass industry, such as sputter processes and laser processing. This approach can not only reduce costs, but also opens up the possibility of separating the production process into the manufacture of semi-finished PV products and their refinement into coloured BIPV modules. For example, semi-finished PV panels could be produced in Asia and the refinement can be done locally in Europe.

The panel-on-demand concept for flexible design of building integrated thin-film photovoltaics requires new processes for glass cutting, a cost-effective and durable colour design, and back-end interconnection of cells to a module. In this publication, we present the development status of three processes for (1) laser-based glass cutting, (2) front contacts with integrated colours in CIGS (using metal-oxide-metal multilayers) and their application on modules together with standard monolithic interconnection, and (3) for back-end interconnection processes for amorphous silicon thin film modules, which are necessary to prepare modules from semi-fabricates of custom size and shape. Together, the three processes allow flexibility in the design of the colour, shape and size of solar façades. In addition, implementation of the concept including just-in-time processing of standard modules into customised modules locally would increase time flexibility, as it would be possible to react to customer wishes and requirements of a building project at short notice.

It has previously been shown that the electrodes with integrated colour can also be applied to amorphous silicon cells and that the principle of back-end interconnection can also be applied to CIGS cells.<sup>7-10</sup> This shows that the concept of flexible design can be implemented for both of the thin-film technologies mentioned.

The results shown here are results from the Solar-era.net project 'Building Integrated Photovoltaics panels on demand'.

## 2 | METHODS

### 2.1 | Laser-based glass cutting

A prototype to cut or separate thin film PV semi-fabricates into custom shape and size was developed. Glass substrates sized up to 1200 mm × 600 mm × 3 mm with both molybdenum coating and a full CIGS layer stack were used for testing. An ultra-short pulse laser from Coherent with a pulse length of ~12 ps, a pulse energy of ~1 mJ at a wavelength of 1064 nm for glass modification, and a CO<sub>2</sub> laser from Coherent for the final separation step were used. Samples were characterized with an optical microscope from Zeiss after cutting.

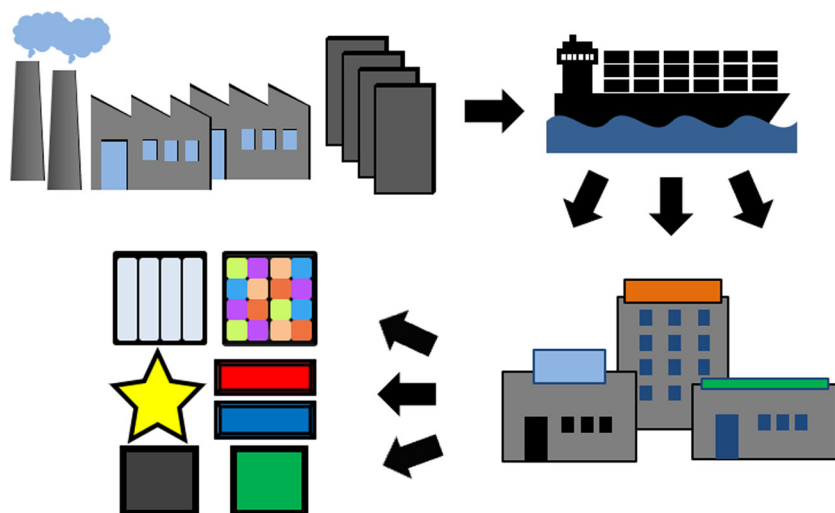


**FIGURE 1** Visualization of flexible and just-in-time adaption of size, shape and colour of mass-produced semi-fabricates possible due to processes for flexible design of solar modules

## 2.2 | Front contact with integrated colour

Oxide/metal/oxide (OMO) electrodes ( $30 \times 30 \text{ cm}^2$ ) were prepared with aluminium-doped zinc oxide (AZO) as the oxide and silver (Ag) as the metal via DC magnetron sputtering at room temperature in an in-line tool (Vistaris 600 by Singulus, Germany). An  $\text{AgO}_x$  wetting layer was used to increase homogeneity and conductivity of the Ag layer.<sup>11</sup> Prior to deposition of the electrodes, the sputter rates of the AZO deposition processes were determined by thickness measurements single-layer reference samples on glass substrates with a relative error of 2%. To determine the deposition rate of silver, samples with a sandwich of two AZO layers with and without a silver layer in-between were prepared. For the very thin silver layers this results in a thickness measurement error of about 1 nm or  $\sim 13\%$ . All layer thicknesses given in Table 2 are calculated from these deposition rates and not measured directly. The thickness given for silver layers includes an  $\text{AgO}_x$  wetting layer of about 1 nm. All deposition parameters can be found in the Tables 1 and 2. The OMO electrodes were applied on semi-finished  $30 \times 30 \text{ cm}^2$  CIGS circuits (pre lamination modules) based on state of the art, Cd-free processes by AVANCIS, leading to aperture efficiencies of up to 19% on small modules.<sup>12</sup>

The modules were structured with P1 and P2 lines and had a reduced AZO front contact thickness of only 200 nm. The front contact was not removed completely in order to keep the optimized and stable absorber/buffer/front contact interfaces and to avoid degradation of the samples during transport. After deposition of the OMO electrode, P3 structuring, edge deletion and lamination of the modules were performed with standard processes of AVANCIS. Afterwards, there were 56 cells on each module with an aperture of  $665 \text{ cm}^2$  including scribes. Four modules with OMO electrodes are presented in this study: one reference module with the OMO electrode tuned for highest current generation, and three coloured modules in blue, red and green.

Current–voltage (IV) characterization was performed with a constant-light solar simulator by Wacom under AM1.5 illumination.

The samples were stabilized under illumination before measurement. As only the four modules listed in Table 2 were used in this study, it was not possible to do any statistical evaluation regarding the accuracy of the measurements. Based on the experience with the setup, we estimate the following error tolerances in relative percent: current  $\pm 0.4\%$ , voltage  $\pm 0.3\%$  and efficiency  $\pm 0.7\%$ . P2 structuring lines were investigated prior to OMO deposition by scanning electron microscope (SEM) with a Zeiss Crossbeam system with a Gemini 2 electron column. Photographs were taken with a Canon DSLR 550D with 18–55 mm lens without any filter in December 2020 at 2 pm under diffuse lighting due to an overcast sky. One-dimensional optical simulations were performed with the software package SCOUT/CODE as described previously.<sup>13</sup> Colour coordinates were calculated from reflection spectra using the python colour science package.<sup>14</sup>

## 2.3 | Back-end interconnection

Amorphous silicon thin film solar cells were used for the development of the back-end interconnection process. A  $\text{SnO}_2:\text{F}$  transparent conductive oxide (TCO) coated glass from Asahi Glass Company (type VU) was used as the substrate, which was wet-chemically cleaned. An amorphous p-i-n silicon layer stack (a-Si:H) with a total thickness of about 300 nm was deposited by Plasma Enhanced Chemical Vapour Deposition (PECVD) on top of the front contact TCO. Subsequently, a magnetron sputtered layer stack of 80 nm AZO, 200 nm Ag and 80 nm AZO was deposited and used as a back-contact system and completes the solar cell structure. The same AZO/Ag/AZO stack was also used during the back-end interconnection process to interconnect neighbouring solar cells on the module (i.e., conductor). For more details regarding the PECVD and sputtering processes, see Agashe et al.<sup>15</sup> and Rech et al.,<sup>16</sup> respectively. In order to realize the back-end interconnection, parts of the layer stack must be selectively removed and spatially resolved insulators must be deposited. The individual layers are removed selectively by laser irradiation through the glass

**TABLE 1** Deposition parameters of the OMO electrodes with integrated colours

Layer	Thickness (nm)	Power (W)	Ar flow (sccm)	O <sub>2</sub> flow (sccm)	Pressure (10 <sup>-3</sup> mbar)	Sputter mode and cathode
AZO top	58–231	3000	290	29	4.5–4.6	DC planar
AZO bottom	30–106	3000	140	0	2.0–2.1	DC planar
$\text{AgO}_x$ (WL)	0.8	200	800	20	8.0–8.1	RF planar
Ag	6.6	700	800	0	7.9–8.0	RF planar

**TABLE 2** Layer thickness for each colour

Colour	Bottom AZO (nm)	$\text{AgO}_x + \text{Ag}$ (nm)	Top AZO (nm)
Reference	30	7.4	58
Blue	91	7.4	196
Red	30	7.4	158
Green	106	7.4	230

Note: Thicknesses were determined from sputter deposition rates of separate samples, resulting in an error of  $\pm 2\%$  for AZO and  $\pm 1 \text{ nm}$  for Ag.

substrate leading to an ablation of the material in scribe lines, parallel across the whole substrate. To achieve material selectivity, nanosecond Q-switched solid-state laser sources with different wavelength of 355 nm and 532 nm were applied. A commercial laser scribing system with X–Y linear stages allowing feed-rates of 1000 mm/s was used for sample translation. A modified commercial 3D printer was deployed for spatially resolved insulator deposition. The printer was equipped with an air dispenser to print the insulator, which consists of a UV curable acrylic resin (bondic®). The resin is printed through a syringe with a nozzle diameter of 1.37 mm. The printing speed as well as the printing air pressure were adjusted to achieve a mass flow that generates a continuous line with width  $\sim 1.4$  mm. Curing of the resin with an UV LED was performed directly after printing.

### 3 | RESULTS AND DISCUSSION

In order to realize the panel-on-demand approach proposed in the introduction, processes to customize semi-fabricated solar modules in regard to size, shape and colour after the initial production are required. We present our findings regarding processes for glass cutting to customize shape in Section 3.1, for front contacts with integrated colour in Section 3.2 and for back-end interconnection in Section 3.3.

#### 3.1 | Glass cutting

A low-damage separation process for the substrate glasses is required for flexible module design. There are existing processes for laser cutting of glass and also laser cutting of silicon wafers has been investigated recently, but the cutting of thin film photovoltaic cells is a novel application.<sup>17,18</sup> The challenge here is not to damage or only minimally damage existing contact and absorber layers when cutting. Laser sources with short pulses in the picosecond and femtosecond range are usually used for such separation processes. The process consists of two stages: first, the substrate glass is perforated or filamented

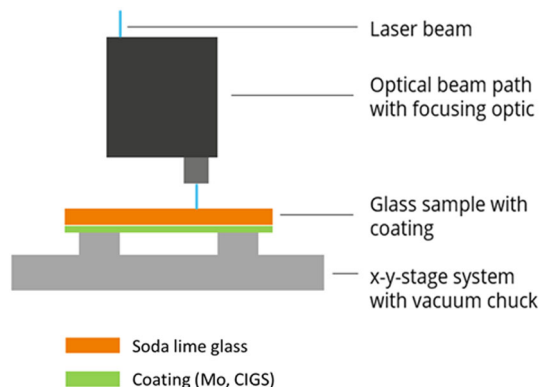


**FIGURE 2** Setup for the separation or cutting of CIGS semi-finished products

with a picosecond laser and a special optical setup to create a pre-determined breaking point. This is followed by the separation process: this can be done either through the use of mechanical forces or through targeted heating with the help of a CO<sub>2</sub> laser of a suitable wavelength. In order not to damage the already existing photovoltaic layers, the processing is carried out from the back of the substrate glass. The coatings on the glass are ablated due to the exit of the filament laser pulses on the rear side of the glass. In Figure 2, a schematic of the setup for our glass cutting system is shown. Appropriate system technology, as described in the method section, was set up in a prototype tool for processing large-area substrates, which is displayed in Figure 3. The tool is capable for flexibly scalable glass substrates. Its main features are presented in Table 3:

Substrate glasses with larger formats can also be processed on appropriately scaled systems due to the flexibility of the laser beam delivery in conjunction with the substrate movement through an axis system. It is also feasible to adapt the process to cut glass substrates with thickness higher than 3 mm by either making multiple passes over the same filament or by employing a laser source with a higher pulse energy and an adapted optical setup. The separation process was first tested with samples of molybdenum on glass and then with the complete CIGS cell stack on glass.

The results achieved on both types of samples were investigated by optical microscopy (see Figure 4) and can be summarized as follows:

1. Good surface and reverse side qualities were achieved, that is, little flaking and few cracks.
2. The side wall quality can also be rated positively, as a homogeneous surface can be seen.

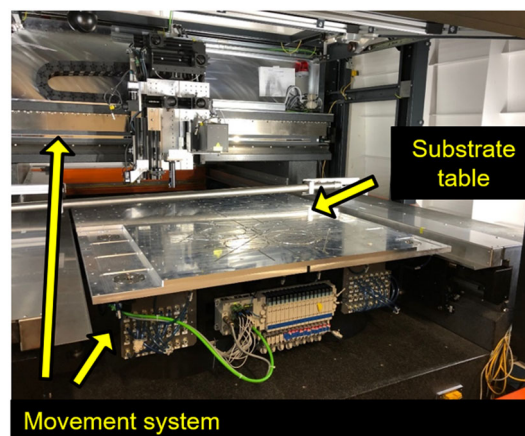


**FIGURE 3** Interior view of the processing room of the prototype

**TABLE 3** Specifications of the prototype tool for glass cutting

Substrate sizes up to GEN5:	1200 × 1400 mm <sup>2</sup>
Max. process speed:	1 m/s
Reproducibility of movement system	±2 μm

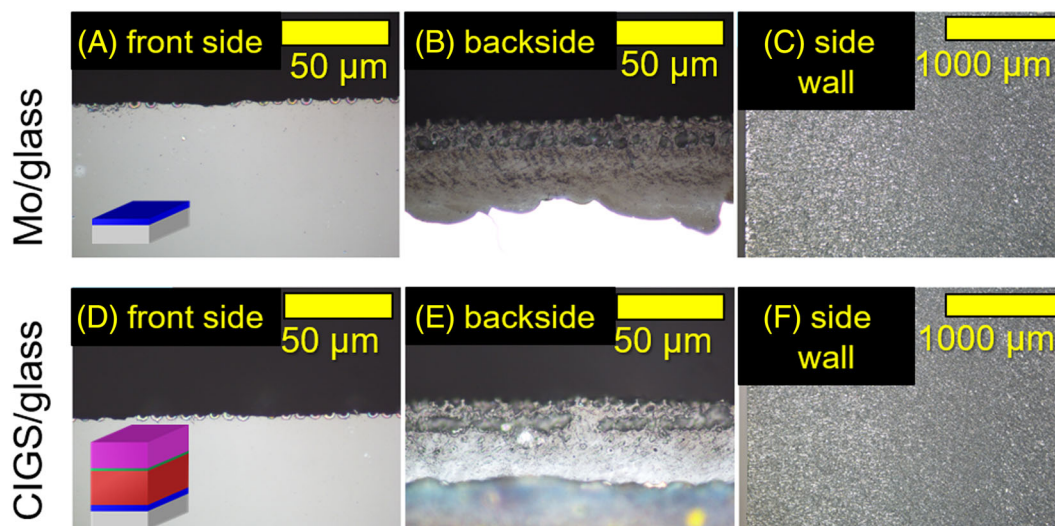


**FIGURE 4** Optical microscopy images of samples after application of the separation process. In the top row Mo/glass samples are shown and in the bottom row CIGS/glass samples. Front and backside are top views on the cutting region

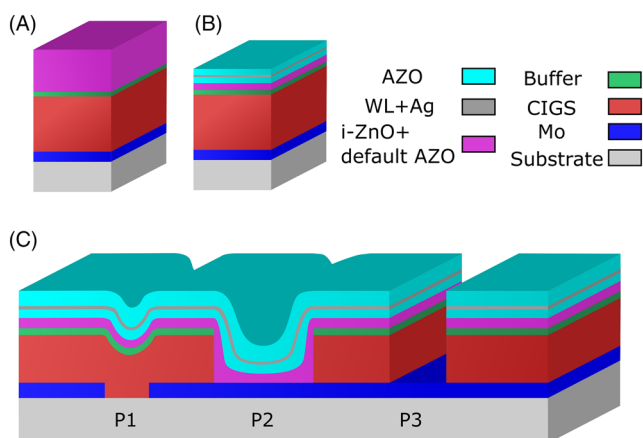


**FIGURE 5** (A, B) Schematic layer stack of a CIGS solar cell with a standard  $\sim 1 \mu\text{m}$  AZO electrode and with an OMO electrode on top of 200 nm standard AZO. (C) Schematic of monolithic interconnection of CIGS modules. OMO electrodes are compatible with the standard processes for both P2 and P3 structuring

- The removal to the Mo and the Mo/CIGS coating is in the range of only  $\sim 50 \mu\text{m}$ , as can be seen in Figure 4B,E. The application of an edge deletion process, as is standard for commercial thin film modules, would ensure a reliable and stable module output.
- As is evident from the optical microscopy results, a separation of the coated glass substrates using a  $\text{CO}_2$  laser has been successfully demonstrated.

Laser cutting methods for glass are common in the glass and display industry. However, to our knowledge, there is no production on industry level of customized modules regarding shape and colour. We have successfully demonstrated the ability of common glass cutting technologies to cut coated thin-film glass substrates in order to customize thin film modules in shape and colour.

### 3.2 | Front contacts with integrated colour

The application of oxide/metal/oxide electrodes instead of the typical front contact TCO layer offers the opportunity to tune the reflected spectrum of the solar cell while maintaining comparable high conductivity and transparency of the electrode.<sup>11,13,19,20</sup> The maxima of the reflection spectrum can be shifted by changing the thickness of the oxide layers to produce a wide range of colours. Here, we report on the fabrication of coloured OMO/CIGS solar modules. The process for preparation of such colouring OMO electrodes, shown in Figure 5B, was introduced previously.<sup>13</sup> In separate study, we reported on processes for improved OMO electrodes by the application of a wetting layer.<sup>11</sup> For the present publication, these improved processes including the  $\sim 1 \text{ nm}$  thick  $\text{AgO}_x$  wetting layer were translated from sample size  $10 \times 10 \text{ cm}^2$  to size  $30 \times 30 \text{ cm}^2$  in an in-line sputter tool, as described in the methods section, to prepare coloured samples. Additionally, standard processes for the monolithic interconnection of cells were applied to verify the compatibility of OMO-electrodes with the current industry standard processes. Thus, we can present here the results for solar modules instead of cells.

Three  $30 \times 30 \text{ cm}^2$  OMO/CIGS modules in blue, green and red and one reference module with an OMO electrode optimized for high current generation were prepared. As can be seen in Figure 6, a homogeneous colour appearance and a barely visible interconnection could be achieved. In Figure 7A, the reflection spectrum of the visible range is shown. The colour is produced by reflection spectra with intensities below 15%, with the maximum at 465 nm for blue, 527 nm for green and 662 nm for red colour. Despite the low reflection intensity, it is clear from both the CIE-diagram shown in Figure 7B and the photograph, that the reflection results in a rich colour expression. The colours look especially vibrant when exposed to direct sunlight. The colour range accessible through OMO electrodes on CIGS cells corresponds approximately to a circular area whose circumference passes through

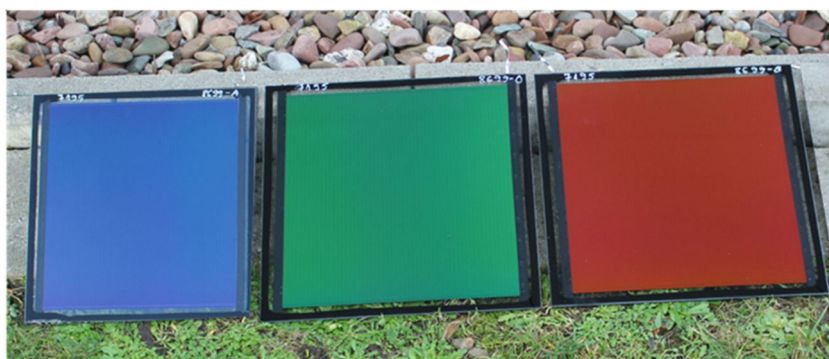


**FIGURE 6** Photograph of coloured OMO/CIGS modules with total size of  $30 \times 30 \text{ cm}^2$  each. Due to edge deletion and contact ribbons there are 56 cells on each module with an aperture area of  $665 \text{ cm}^2$ . The photo was taken in December at 2 pm under diffuse lighting due to an overcast sky

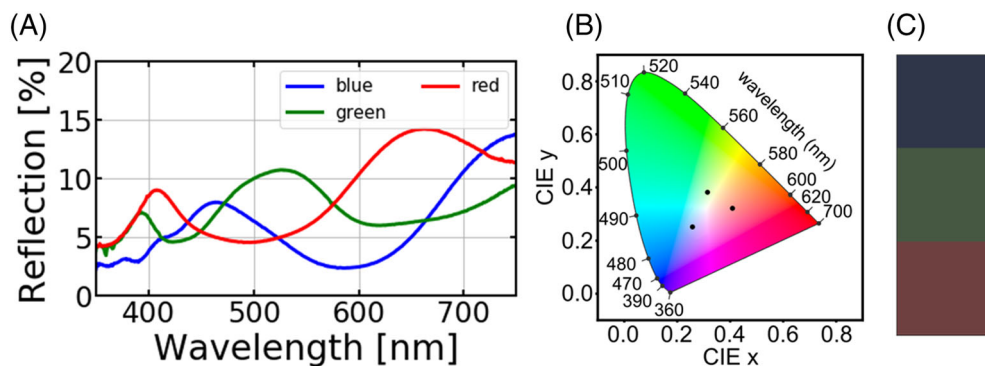


**FIGURE 7** (A) Reflection in the visible range of the coloured OMO/CIGS modules. (B) 1931 CIE chromaticity diagram with the colour coordinates of the samples calculated from the measured spectrum. (C) Colours drawn based on RGB values calculated from the measured spectrum

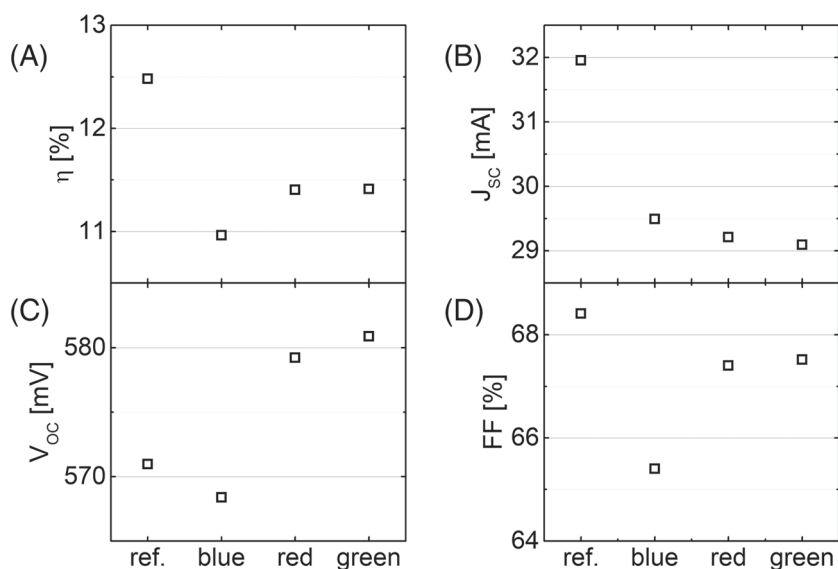


**FIGURE 8** Current-voltage characteristics of the reference module and the three coloured modules. Efficiencies of 12.4% and 10.9–11.4% were achieved for the reference module and coloured modules, respectively. While the blue colour allows for the highest current generation of the all colours, losses in  $V_{oc}$  and FF, most likely due to shunts, resulted in a slightly lower overall efficiency of the blue module

the colour dots shown in Figure 7B. Thus, the flexible colour design mentioned in the introduction can be implemented with OMO electrodes. The efficiency, short circuit current, open circuit voltage per cell and fill factor extracted from solar simulator measurements are shown in Figure 8. With the present modules, efficiencies of 10.9–11.4% were achieved for the coloured modules and 12.4% for the reference module. Therefore, the efficiency was only decreased by about 1% (abs.) due to the tuning of the OMO electrodes for specific colours. Compared with an optimized AZO-only front electrode the efficiency however is still reduced by more than 20% relative. Additionally, it can be

noted how the OMO technology has improved compared to the results published previously with a efficiencies of 8.1–8.5% for coloured OMO/CIGS solar cells.<sup>13</sup> The main improvement is the increased short-circuit current density with, for example,  $29.5 \text{ mA/cm}^2$  for the blue module compared with  $20.9 \text{ mA/cm}^2$  for the blue cell previously published. This improvement was possible due to two effects: First, the application of the  $\text{AgO}_x$  wetting layer was successfully integrated in the OMO electrode also on module level, resulting in both lower sheet resistance and higher transmission of the electrode.<sup>11</sup> Second, in contrast to the previously studied cells, the modules presented here were

laminated with a cover glass. Due to the successively decreasing refractive indices of AZO, encapsulation foil, glass and air, which are  $n_{\text{AZO}} \sim 2.0$ ,  $n_{\text{foil}} \sim 1.7$ ,  $n_{\text{glass}} \sim 1.6$  and  $n_{\text{air}} \sim 1.0$ , the encapsulation reduces the reflection similar to an antireflection layer.<sup>13</sup> Consequently, more light is transmitted into the cell and a higher current is generated. The variation in short-circuit current density among the coloured solar cells can be attributed to the different reflection spectra and the influence of the different AZO layer thicknesses on the absorption. We previously reported on the influence of the silver layer on the sheet resistance of OMO electrodes; therefore, it can be concluded that the AZO layer thickness has only a minor impact on the sheet resistance of the modules.<sup>11</sup>

Furthermore, there is no indication for any increased series resistance or shunting of the modules. It follows that the OMO electrode is compatible with the standard monolithic interconnection, specifically the P2 and P3 lines and processes (see Figure 8C), which is not a trivial task. At the P2 line, the front contact has to provide a sufficiently conductive contact to the back contact. In the case of CIGS cells, the approx. 8 nm thick silver layer within the OMO electrode has to bridge a 2  $\mu\text{m}$  deep cliff due the removal of the absorber layer for the P2 line. However, as the SEM images in Figure 9 show, the incline between front and back contact is below 20°. Therefore, the OMO layer is only slightly stretched at the incline and a sufficient contact can be established. The P3 line was prepared by standard mechanical scribing. In contrast to the P2 line, electrical contacts between front and back contact have to be avoided here. Three of the four modules show no indication for shunts. As there are 56 cell stripes per module it can be concluded that the standard P3 process is also compatible with the OMO electrode.

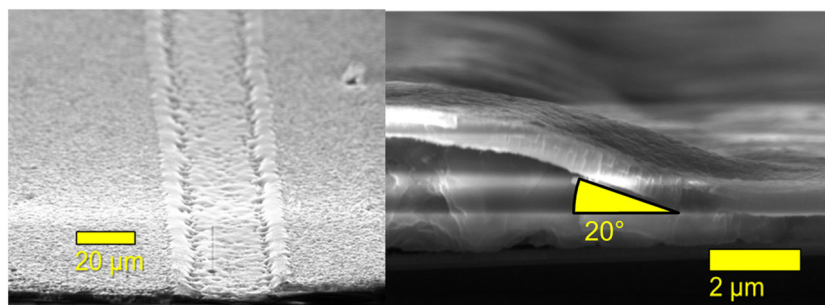
The performance results achieved here, namely, an efficiency of 10.9–11.4% and an estimated loss in efficiency of approx. 20% relative to comparable non-coloured modules with a standard front contact, are in line with results reported in literature. Kutter et al. reported power losses ranging from 6% to 31% for different colour technologies including a structural colour implemented on the front glass (3–7% power loss).<sup>21</sup> Jolissaint et al. reported on another structural colour integrated in the cover glass with also approx. 7% power loss.<sup>22</sup> A direct comparison can be made with commercially available, coloured CIGS modules from AVANCIS, which are offered with aperture efficiencies of 12.6–13.7% for various colours.<sup>23</sup> However, an advantage of the OMO-coloured modules presented here is that the colour can be chosen from a wide range by simply adapting the thickness of the front contact AZO

layers directly on the module, which is then completely protected by the cover glass. Furthermore, OMO electrodes can also be employed for other thin-film PV technologies like amorphous silicon solar cells, where they have been employed both for the front and back electrode.<sup>7–9</sup> Another important aspect for a commercial application is reliability. Theelen et al. conducted damp-heat tests of OMO electrodes on glass substrates and concluded that in the absence of humidity, which is the normal condition below an intact cover glass of a solar module, OMO layers were very stable.<sup>24</sup>

### 3.3 | Back-end interconnection

In the previous section the standard monolithic interconnection was shown to be working in combination with coloured CIGS modules. In this section, we focus on another interconnection technology to fully implement the panel on demand approach, the back-end interconnection. It has the advantage that the interconnection process can be performed separately (regarding both time and space) from the layer deposition processes. Furthermore, it allows for the back-end preparation of solar modules in custom shape and size, as the element in question can be structured in such a pattern that the required uniformity of current production in each cell stripe can be guaranteed. To further clarify this point, let us examine the hypothetical case of a triangle shape cut from a standard module. Here the cell stripes would not have the same area, and the current output would be limited by the smallest cell area. By applying a customized structuring with module stripes or cells of equal area, the full current could also be extracted from such a triangular module. Furthermore, it is possible to a certain extent to structure modules of different shapes or sizes in such a way that series connection is possible. The back-end interconnection approach used in this study, which was already developed in CIGS thin film technology,<sup>25,26</sup> is demonstrated on amorphous silicon thin film solar cells and is shown in Figure 10. At the beginning, the front contact layer, the solar cell absorber including the charge carrier separating junction and the back contact are deposited. Afterwards, a laser patterning step P1 is performed to separate the area into individual solar cells by local removal of the whole layer stack. Then the generated laser groove is filled with an insulator (UV curable acrylic resin), to protect the front contact from electrical connections. Next, a second laser patterning step P2 is used to expose the front contact locally beside the P1 cut, followed by the deposition of a conductor

**FIGURE 9** SEM image of P2 structuring line before OMO deposition top view (left) and cross section (right). In the second image three layers are clearly recognizable: The back-contact layer, the absorber layer, and the front contact. The flat angle of the sloping flank between the front contact and the back contact allows sufficient contact with OMO electrodes

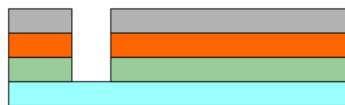




1) Complete Cell Deposition



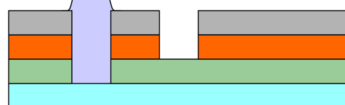
2) Laser Patterning P1



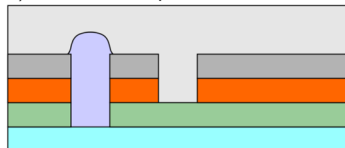
3) Printing Insulator



4) Laser Patterning P2



5) Conductor Deposition



6) Laser Patterning P3

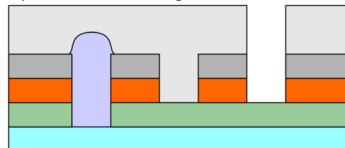


**FIGURE 10** Deposition and laser patterning sequence to fabricate the back-end interconnect from complete cell to fully patterned module

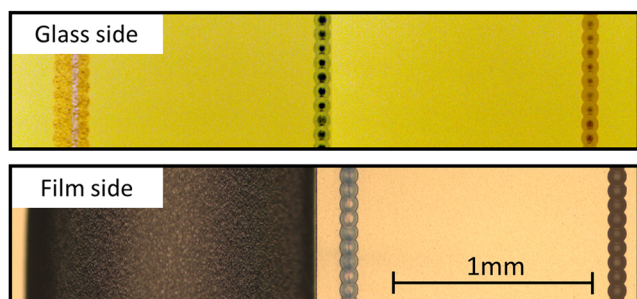


**FIGURE 11** (Top) Optical micrograph of the interconnection area of the back-end interconnected module. The image was digitally post-processed so that details are better visible. (Bottom) Optical micrograph of the film side of the same module. Both images (top and bottom) were composed from two single images

on the whole substrate area. The conductor consists of the same layer stack already used for the back contact. However, for future applications of the back-end interconnection in the panel on demand concept based on coloured CIGS modules, the conductor can favourably be fabricated from the OMO layer stack. Finally, a last laser patterning step P3 is used to remove the shortcut between front contact and back contact and to finish the series interconnection.

Figure 11 shows an optical micrograph of the amorphous thin film module with back-end interconnection. A cell stripe width of 10 mm (active area width + interconnection area width) and a cell stripe height of 80 mm was chosen for the module. The top shows an image of the glass side, whereas the bottom image is taken from the film side of the module. The glass side image shows a P1 groove which actually consists of two grooves. Here first an ablation of the absorber as well as the back contact was performed with the laser source operating at 532 nm wavelength. Thereafter the front contact was also removed

within the first ablation groove with an ablation utilizing the laser source operating at 355 nm. The breakdown into two individual ablation steps was used to avoid shunts by the laser process. To ensure that the ablation of the front contact is positioned within the ablation of absorber and back contact, the later was generated by four ablation grooves touching each other.

Beside the P1 process, Figure 11 also shows the exposure of the front contact (P2) in the middle and the isolation step (P3) on the right-hand side. Both processes were performed with similar laser processes utilizing the laser source with a wavelength of 532 nm. The distances between the patterning steps P1, P2 and P3 were chosen such that the printing process only needs an accuracy in the millimetre range. This was necessary because the accuracy of the used 3D printer suffers from a missing fiducial system. The large gaps between the patterning grooves led to a total interconnection width of  $\sim 2.7$  mm and thus also a relative area loss of  $\sim 27\%$ .

In Figure 12, the electrical characteristics of 12 reference cells and 8 module cell stripes are compared. All samples were deposited in the same deposition runs. In order to easily compare the curve of both device types, the cell stripe currents were normalized to the active area of the cell stripes.

The results show a very good agreement between the characteristic of the reference cells and the cell stripes. Both achieve equivalent short circuit current densities  $J_{sc}$  above  $15 \text{ mA/cm}^2$ . The fill factor of the cell stripes suffers a little bit compared to the reference cell. This is most probably due to higher series resistance, which is attributed to a stronger influence of the TCO resistance in the module configuration. Here the current is handed over from the TCO to the highly conductive metal layer only at one side of the cell stripe. In contrast the TCO of the square reference cell (size  $1 \text{ cm}^2$ ) is contacted with a highly conductive metal at each side of the cell perimeter.

**FIGURE 12** J/V characteristic of 12 individual reference cells (left) and 8 module cell stripes (right). The reference cells were deposited in the same deposition runs as the module. In order to compare the results of the reference cells and the module cell stripes, the active area characteristic of the cell stripes is plotted

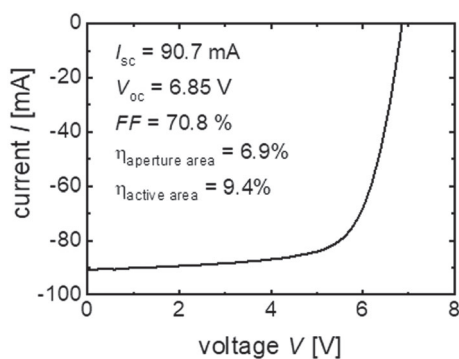
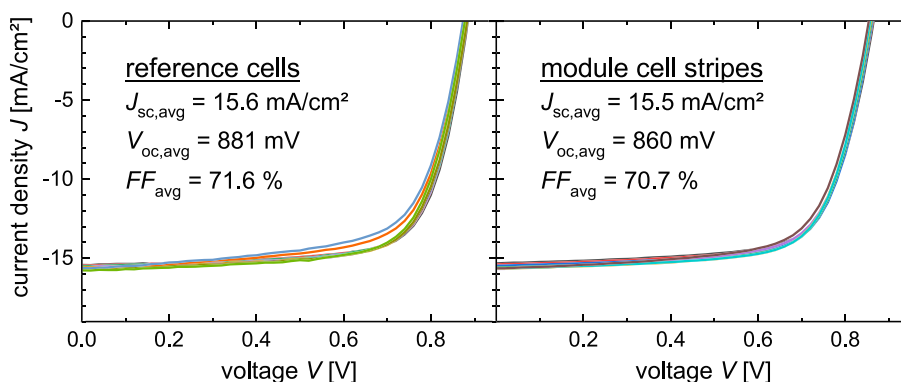


**FIGURE 13** I/V characteristic of the back-end interconnected amorphous silicon thin film module. The module exhibits a high fill factor above 70% which indicates low electrical losses due to the interconnection. This results in an active area efficiency of 9.4%

The largest loss is found for the open circuit voltage  $V_{oc}$ . Here the cell stripes show in average a loss of 21 mV compared with the reference cells. The origin of this loss is not clear yet. However, we do not attribute the  $V_{oc}$  loss to the back-end series interconnection, since problems here, for example, due to shunts would also negatively influence the fill factor to a much greater extent than evident in the results.

Figure 13 shows the I/V characteristic of the whole back-end interconnected amorphous silicon thin film module. The fill factor is above 70% which is a sign for low electrical losses in the interconnection. Overall the module achieves an active area efficiency of 9.4%. However, due to the large width of the interconnection region and the related area losses, the aperture area efficiency of 6.9% is well below the active area efficiency. Here especially better accuracy of the printing processes gives room for future reduction of the area related losses. In addition, further investigations should be carried out to study the long-term stability of the new interconnection structure compared to conventional interconnection based only on laser structuring and/or mechanical scratching.

The back-end interconnection approach we have implemented for amorphous silicon thin film modules is also applicable for other thin film technologies like CIGS, cadmium-telluride or perovskites. The approach has already been implemented for CIGS,<sup>25,26</sup> where a transparent conductor was used due to the substrate concept. Comparing our results

with literature, the most obvious difference is the high fill factor of over 70% we achieved, whereas in literature values around 60% and well below are usually found.<sup>10,25–29</sup> Despite these results reported in literature, to our knowledge there is no production on industry level of customized modules regarding shape and colour and no post-interconnection process after the deposition of all contact and active layers. Up to now the serial interconnection using laser scribes after single deposition steps remains the standard for thin film solar modules.

## 4 | CONCLUSION

A panel-on-demand procedure for refinement of semi-fabricates to customized modules was proposed to allow for flexible design of building integrated thin-film photovoltaics. When fully realized in the industry, standard semi-finished thin film modules would be mass produced in a first step and then shipped to local refinement centres. There an architect could order modules of arbitrary shape and colour. Following the commission, the semi-fabricates would be cut in the desired shape, then an OMO-electrode with the requested colour would be applied, before the elements would be structured into modules via the back-end interconnection process. Three processes to implement this approach were demonstrated in this study, namely a laser-based process for cutting semi-fabricates, an oxide/metal/oxide front contact electrode with integrated colour and a back-end interconnection process to allow for structuring modules from elements in custom shape. The laser cutting process resulted in samples where damage was only visible within a maximum distance of 50  $\mu\text{m}$  from the cut. The application of OMO electrodes together with standard monolithic interconnection resulted in coloured modules in red, green and blue with only 1% absolute less efficiency compared to a reference module. A back-end interconnection process was demonstrated on a-Si:H cells which performed similar to the respective reference cells when the active area loss was taken into account. Further optimization of these processes to increase the efficiency of the prepared modules may be necessary for commercial adaption, however technical feasibility has been demonstrated. Additionally, the combination of all three processes needs to be shown, though each process could already be adopted on its own and separately at this stage. All processes presented here are based on tools which are typically present

in the solar or glass industry, which allows for an easier adaption of the processes by commercial manufacturers. The panel-on-demand strategy may allow for a streamlined production of customized modules and a lower cost for aesthetically pleasing, fully building integrated solar modules.

## ACKNOWLEDGEMENTS

The authors gratefully acknowledge Maximilian Götz-Köhler for additional proof reading of the article and AVANCIS GmbH for providing the CIGS samples used for the coloured CIGS modules as well as for measurements.

The authors gratefully acknowledge the funding of BMWi (FKZ0324130A) in the German-Dutch ERANET collaboration project BIPVpod.

## ORCID

Nils Neugebohrn  <https://orcid.org/0000-0002-3335-7861>

## REFERENCE

- Abergl T, Dean B, Dulac J. Towards a zero-emission, efficient, and resilient buildings and construction sector: Global Status Report 2017.
- Eggers J-B, Behnisch M, Eisenlohr J, Poglitsch H, Kuhn TE. PV-Ausbauerfordernisse versus Gebäudepotenzial: Ergebnis einer gebäudescharfen Analyse für ganz Deutschland. In: *PV-Symposium*; 2020.
- Berliner Abgeordnetenhaus. Solargesetz Berlin; 2021.
- Kuhn TE, Erban C, Heinrich M, Eisenlohr J, Ensslen F, Neuhaus DH. Review of technological design options for building integrated photovoltaics (BIPV). *Energy and Buildings*. 2021;231:110381. doi:10.1016/j.enbuild.2020.110381
- Corti P, Bonomo P, Frontini F, Mace P, Bosch E. *Building Integrated Photovoltaics: A Practical Handbook for Solar Buildings' Stakeholders*; 2020.
- Wilson GM, Al-Jassim M, Metzger WK, et al. The 2020 photovoltaic technologies roadmap. *J. Phys. D: Appl. Phys.* 2020;53(49):493001. doi:10.1088/1361-6463/ab9c6a
- Neugebohrn N, Gehrke K, Götz-Köhler M, Vehse M. Customized, aesthetically appealing photovoltaic modules at reasonable price for the BIPV mass market. In: 13th Conference on Advanced Building Skins: 1–2 October 2018, Bern, Switzerland. Wilen (Sarnen): Advanced Building Skins GmbH; 2018:689–693.
- Lim JW, Kim G, Shin M, Yun SJ. Colored a-Si:H transparent solar cells employing ultrathin transparent multi-layered electrodes. *Solar Energy Materials and Solar Cells*. 2017;163:164–169. doi:10.1016/j.solmat.2017.01.017
- Kim G, Lim JW, Shin M, Yun SJ. Bifacial color realization for a-Si:H solar cells using transparent multilayered electrodes. *Solar Energy*. 2018;159:465–474. doi:10.1016/j.solener.2017.11.019
- Wagner M, Würz R, Kessler F, Rahm A, Scheit C, Ragnow S. Post-monolithic interconnection of CIGS solar cells. In: 24th European Photovoltaic Solar Energy Conference, 21–25 September 2009; Hamburg, Germany; 2009:2986–2988. doi:10.4229/24thEUPVSEC2009-3BV.5.40.
- Neugebohrn N, Osterthun N, Götz-Köhler M, Gehrke K, Agert C. Improved metal oxide electrode for CIGS solar cells: the application of an AgOX wetting layer. *Nanoscale Res Lett*. 2021;16(1):50. doi:10.1186/s11671-021-03506-1
- Stoelzel M, Algasinger M, Zelenina A, Weber A, Palm J. Absorber optimization in CIGS modules with a sputtered ZnOS buffer layer at 19% efficiency. In: 36th EU PVSEC 2019; 2019.
- Neugebohrn N, Gehrke K, Brucke K, Götz M, Vehse M. Multifunctional metal oxide electrodes: colour for thin film solar cells. *Thin Solid Films*. 2019;685:131–135. doi:10.1016/j.tsf.2019.06.012
- Mansencal T, Mauderer M, Parsons M, et al. *Colour 0.3.16*. Zenodo; 2020.
- Agashe C, Kluth O, Schöpe G, Siekmann H, Hüpkens J, Rech B. Optimization of the electrical properties of magnetron sputtered aluminum-doped zinc oxide films for opto-electronic applications. *Thin Solid Films*. 2003;442(1-2):167–172. doi:10.1016/S0040-6090(03)00966-0
- Rech B, Roschek T, Repmann T, Müller J, Schmitz R, Appenzeller W. Microcrystalline silicon for large area thin film solar cells. *Thin Solid Films*. 2003;427(1-2):157–165. doi:10.1016/S0040-6090(02)01210-5
- Kondratenko VS. Method of splitting non-metallic materials. Expired - Fee Related (US5609284A); 1997. <https://patents.google.com/patent/us5609284a/en>
- Korzeniewska E, Tomczyk M, Pietrzak Ł, et al. Efficiency of laser-shaped photovoltaic cells. *Energies*. 2020;13(18):4747 doi:10.3390/en13184747
- Guillén C, Herrero J. TCO/metal/TCO structures for energy and flexible electronics. *Thin Solid Films*. 2011;520(1):1–17. doi:10.1016/j.tsf.2011.06.091
- Yun J. Ultrathin metal films for transparent electrodes of flexible optoelectronic devices. *Adv Funct Mater*. 2017;27(18):1606641. doi:10.1002/adfm.201606641
- Kutter C, Bläsi B, Wilson HR, et al. Decorated building-integrated photovoltaic modules: power loss, color appearance and cost analysis. In: 35th European PV Solar Energy Conference and Exhibition; 2018: 1488–1492.
- Jolissaint N, Hanbali R, Hadorn J-C, Schüler A. Colored solar façades for buildings. *Energy Procedia*. 2017;122:175–180. doi:10.1016/j.egypro.2017.07.340
- Avancis Skala Modules - Technical Data Sheet. [https://www.avancis.de/wp-content/uploads/2021/07/FE\\_PD\\_SKALA\\_DATASHEET\\_DE\\_2021-07\\_Web.pdf](https://www.avancis.de/wp-content/uploads/2021/07/FE_PD_SKALA_DATASHEET_DE_2021-07_Web.pdf)
- Theelen M, Hagedoorn C, Götz-Köhler M, Weeber A, Neugebohrn N. Damp heat induced degradation mechanisms occurring in coloured oxide/metal/oxide films for thin-film solar cells. *Thin Solid Films*. 2021;138711.
- Gevaerts VS, Biezemans AF, Mannetje HHI, Linden H, Bosman J. Back End Monolithic Serial Interconnection Technology for CIGS with Shunt-free Laser Scribing and Inkjet Printing. In: 2018 IEEE 7th World Conference on Photovoltaic Energy Conversion (WCPEC) (A Joint Conference of 45th IEEE PVSC, 28th PVSEC & 34th EU PVSEC). IEEE; 2018.
- Gevaerts V, Biezemans A, Mannetje H, Bosman J, Linden H. Inkjet printing assisted monolithic interconnection of CIGS using shunt-free laser scribing. In: 2020 47th IEEE Photovoltaic Specialists Conference (PVSC). IEEE; 2020.
- Crozier ML, Brunton AN, Abbas A, et al. One step thin-film PV interconnection process using laser and inkjet. In: 2013 IEEE 39th Photovoltaic Specialists Conference (PVSC). IEEE; 2013.
- Gilot J, Emelin B, Galagan Y, Mandamparambil R, Andriessen R. Ultimate form freedom in thin film solar cells by postmanufacture laser-based processing. *JPE*. 2015;5(1):57210. doi:10.1117/1.JPE.5.057210
- Fields JD, Pach G, Horowitz K, Stockert TR, Woodhouse M, van Hest M. Printed interconnects for photovoltaic modules. *Solar Energy Materials and Solar Cells*. 2017;159:536–545. doi:10.1016/j.solmat.2016.09.024

**How to cite this article:** Neugebohrn N, Haas S, Gerber A, et al. Flexible design of building integrated thin-film photovoltaics. *Prog Photovolt Res Appl*. 2022;1-10. doi:10.1002/pip.3568